AIMS Biophysics

AIMS Biophysics, 13(1): 29−52.
DOI: 10.3934/biophy.2026003
Received: 07 November 2025
Revised: 25 January 2026
Accepted: 03 February 2026
Published: 11 February 2026

http://www.aimspress.com/journal/biophysics

Research article

Biophysical impact of custom shield materials and apertures on electron beam dosimetry: a Monte Carlo study for clinical applications

Huda Haddad*

Department of Applied Physics, Tafila Technical University, Tafila, 66110, Jordan

* **Correspondence:** Email: huda.haddad@ttu.edu.jo; Tel: +0096232251346; Fax: +962-3-225-0002.

Abstract: *Purpose*. This study aims to evaluate how different shield materials and aperture sizes impact dosimetric properties within the planning target volume (PTV) across various electron beam energies. *Material and Methods*. Monte Carlo simulations were performed using a 30 × 30 × 30 cm^3 solid water phantom covered with a custom bolus-shield assembly. The phantom was irradiated with 6, 9, and 16 MeV electron beam energies. Shield materials included polylactic acid (PLA), acrylonitrile butadiene styrene (ABS), and lead alloy, while the bolus was made of ABS. Three configurations were tested, each pairing a fixed 0.5 cm thick ABS bolus with one of the shield materials (thicknesses were adjusted based on material properties). For each configuration, aperture sizes of 2 × 2, 5 × 5, and 8 × 8 cm^2 were evaluated. Reference simulations were conducted for each energy using a 0.5 cm ABS bolus covering the entire phantom. *Results*. Our findings demonstrate that although ABS and PLA require thicker layers and result in wider penumbras than other materials, they are promising shield materials for low- and medium-energy electron beams. These materials improved surface dose coverage, offered superior deep-tissue protection, and eliminated dual hot spots yielding more favorable distributions. Moreover, sensitivity tests confirmed the model's robustness against setup errors up to ± 5°. However, larger angles introduced obliquity effects, establishing a 5° tolerance limit for reliable clinical applications. *Conclusion*. This study demonstrates that traditional lead shields can be effectively replaced by a custom 3D-printed ABS or PLA unit that functions simultaneously as a bolus and shield. This approach is particularly effective for low and medium electron energies with small-to-moderate apertures, where it enhances surface dose and protects deep tissues more effectively. Ultimately, these findings confirm that tissue-equivalent polymer shields can satisfy clinical radiobiological requirements, offering a viable, non-toxic alternative to lead to optimizing patient safety during superficial cancer treatments.

Keywords: shield; bolus; ABS; PLA; lead; electron radiotherapy

1. Introduction

Shielding materials in electron radiotherapy play a crucial role in protecting surrounding healthy structures by ensuring that radiation is focused only to the target while attenuating the beam elsewhere. Traditionally, lead and low melting-point alloys (LMA) have been used clinically for many years. Lead remains the clinical standard due to its high density and malleability, but its toxicity creates significant challenges regarding staff safety and waste disposal. This has driven a search for non-toxic easier-to handle alternatives [1].

Consequently, recent research has pivoted toward high-density composites and 3D- printed solutions that offer patient-specific conformity without the occupational hazard associated with lead. For example, an investigation into tungsten-containing rubber (STR) shows that flexible composites can achieve penumbral sharpness that exceeds that of standard metal block. Crucially, analysis of bremsstrahlung emission at the depth of maximum dose (d_{max}) found that the X-ray contamination under these tungsten-rubber shields was comparable to standard LMA. This confirms that flexible composite materials can offer superior field shaping without compromising shielding safety [2].

Similarly, innovations, such as transparent acrylic eye shields, address patient safety in a different way; they preserve vision, thereby reducing fall risks during treatment, while still providing effective dose attenuation [3]. Additionally, optimization studies using Monte Carlo simulations (MC) have shown that multi-layered composite designs can significantly reduce electron backscatter compared to using high-Z materials alone [4]. Taken together, these findings signal a shift toward customizable, non-toxic shielding, underscoring the need to rigorously validate the dosimetric properties of these emerging materials.

On the other hand, the electron bolus is an essential tool for optimizing dose delivery. Its primary clinical applications include enhancing surface dose, compensating for irregular patient contours to ensure dose homogeneity across the planning target volume (PTV), and modulating beam penetration to spare deeper healthy tissues [5]. Bolus materials are commonly constructed from tissue-equivalent substances with a density of approximately 1 g/cm^3. A variety of bolus materials are available for clinical use, including water, beeswax, paraffin, polylactic acid (PLA), and acrylonitrile butadiene styrene (ABS) [6−8]. These materials are commonly utilized materials for 3D printing boluses using fused deposition modelling (FDM). This technology enables the creation of high-quality and precise boluses, capable of reaching dimensions as large as $30 \times 30 \times 30\ cm^3$ [9−12].

Recent advancements in fabrication technology have enabled the development of both bolus and shield devices addressing issues such as the toxicity of lead in shielding and the poor conformity of standard boluses. Diaz-Merchan et al. demonstrated that 3D-printed materials can be optimized for homogeneity and air-gap reduction, showing excellent agreement with MC simulations [8]. Building on this, Lee et al. applied these concepts clinically, showing that modulated electron bolus significantly improved conformity and reduced heart and lung doses in breast cancer boost treatments [13]. Regarding shielding, Herchko et al. compared 3D-printed collimators to traditional brass for 6 and 9 MeV electron beams, confirming their ability to sharpen penumbra and spare superficial tissues [14].

In electron beam radiotherapy, a customized shield with an aperture is directly applied to the skin, encompassing the bolus. A primary concern in treatment planning is achieving optimal target dose coverage within the PTV. Additionally, minimizing the lateral dose at the PTV's edges is another challenge. This is influenced by factors, such as electron beam energy, skin collimation, and bremsstrahlung radiation from the shielding material, which can potentially compromise treatment accuracy [15,16].

The dosimetric characterization of small electron fields remains a critical challenge in modern radiotherapy due to the loss of lateral electronic equilibrium. Recent studies by Vendanzio et al. and Han et al. confirm that as the field aperture decreases below the lateral scattering range of the electrons, the output factor drops sharply and the depth of maximum dose (d_{max}) shifts toward the skin surface [17,18]. These perturbations are often not accurately modeled by standard treatment planning systems, which tend to overestimate the dose in the absence of specific small-field corrections [18]. Consequently, accurate experimental verification and MC modeling, as performed in this study, are essential to ensure patient safety when using custom shielding cutouts. Despite significant advancements in understanding shields and bolus materials individually, a substantial gap remains regarding their combined effects. In current clinical practice, bolus and shielding are implemented as separate entities, one applied to the skin and the other mounted in the applicator. This physical separation is problematic; it risks introducing air gaps, complicates setup, and overlooks the complex dosimetric interplay between the components, particularly in small fields where lateral electronic equilibrium is lost [19]. To address this, our study proposes integrating the shield and bolus into a single unit and evaluating their combined impact using MC simulation.

Monte Carlo methods have become the standard for such dosimetric inquiries. For instance, Kong et al. used the Geant4 code to model electron beam transport, ultimately identifying polystyrene and glycerol as optimal bolus materials based on dose deposition in deep tissues [20].

Similarly, Diaz-Merchan et al. employed Geant4 to characterize "BolusCM" a novel material for electron radiotherapy. Their validation against experimental measurements at 6–16 MeV confirmed the material's cost-effectiveness and clinical viability compared to the commercial options [21]. While the prementioned studies relied on Geant4, other researchers have utilized the EGSnrc, the code selected for this work. For instance, Alhamada et al. investigated the shielding disks in intraoperative electron radiation therapy by comparing simulated and measured percentage depth dose (PDD) curves across four clinical materials. They established Al/Pb as the superior shielding combination [4].

MC simulations offer a significant advantage over physical measurements for determining dose distributions, making them a valuable tool for advancing this research. This method eliminates the risk of radiation exposure for clinicians during experimental dose profile measurements. Furthermore, MC significantly reduces the time and effort required for measuring beam profiles while minimizing the positioning uncertainties inherent in experimental studies. They minimize human errors that can occur during experimental setup. Simulation results accurately account for electron scattering in low-energy beams and electron disequilibrium effects in high-energy beams [16,22−24].

The primary goal of this work is to quantify how shielding materials affect dosimetry when placed directly around a bolus of varying sizes. We investigated several key variables, including electron energy, shield material, and the aperture area (specifically matching the bolus size), to assess their combined effect on PTV dose coverage. By better understanding these parameters, we aim to provide data that help clinicians optimize treatment planning and reduce setup times, ultimately leading to safer and more accurate treatment delivery.

2. Materials and methods

2.1. Monte Carlo simulation

MC simulations were performed using the electron gamma showers (EGSnrc) code. EGSnrc is an advanced software toolkit representing a significant evolution of the original EGS package developed at Stanford Linear Accelerator Center (SLAC) in the 1970s. Developed by Kawrakow and Rogers, EGSnrc was designed to simulate the transport of photons, electrons, and positrons through matter, covering a kinetic energy range of 1 keV to 10 GeV. EGSnrc is used in the calculation to quantify correction factors or perturbation effects, as well as in radiotherapy to validate commercial treatment planning systems, calculate precise absorbed doses, and characterize brachytherapy sources [25].

2.1.1. Materials

The materials investigated in this study are ABS, PLA, and lead alloy. The PEGS4 code was used to generate the material cross-section data required for the simulations. For ABS and PLA, the density data needed for PEGS4 code was derived using the National Institute of Standards and Technology (NIST) ESTAR database [26]. For the lead alloy, the density data was obtained from the standard EGSnrc library based on definitions by the International Commission on Radiation Units and Measurements (ICRU). Table 1 summarizes the parameters used to create the material cross-section files, including elemental composition, density, and the energy range for both electrons and photons.

Table 1. Input parameters used for PEGS4 data generation.

Materials	Elemental composition (%) [5, 3, 26]	Density (g/cm^3)	Energy (MeV)	
			Photon	Electron
PLA	C (50); O (44.46); H (5.54)	1.24	0.010−20.000	0.521−20.511
ABS	C (84.68); H (7.93); N (7.39)	0.9		
Lead alloy	Pb (0.8); Sb (0.15); Sn (0.05)	10.04		

2.1.2. Beam simulation

2.1.2.1. Linac head simulations

Electron beams with nominal energies of 6, 9, and 16 MeV were simulated using models of two linear accelerators: Varian Clinac 2100C (6 and 9 MeV) and Philips SL75-20 (16 MeV). These units were accurately modeled using manufacturer specifications and by referencing studies demonstrating strong agreement between simulation and experimental data [27−29].

To simulate the Varian Clinac 2100C head, we utilized the BEAMnrc code [28]. The simulations source was defined using ISOURC 21 (Full Phase-space Beam Data, incident on any CM). Validated phase-space files were used for both 6 MeV (Varian_Clinac_2100CD_6MeV_10×10. IAEAphsp) and 9 MeV (Varian_Clinac_2100CD_9MeV_10×10.IAEAphsp) beam energies [30]. These sources were introduced into the model at the level of the secondary collimators. Therefore, the geometric configuration focused on the secondary collimator jaws, the multi-leaf collimator, and the exit window.

For the 16 MeV simulation of the Philips SL75-20, the simulation source ISOURCE 0 (Parallel Beam from the Front) was configured as a monoenergetic, parallel beam with a radius of 0.1 cm. Upon passing through the exit window and primary collimator, the electron beam was broadened by a composite scattering foil. This component was modeled using layers of lead and copper, shielded by mild steel. The beam transport then continued through the monitor chamber, shielding ring, and mirror. Finally, the treatment field was defined by the main jaws and a square applicator. To ensure accurate penumbra modeling, the applicator was configured with a specific arrangement of five scrapers, comprising two steel and three aluminum layers, positioned at the standard source-to-surface distance (SSD).

For all simulations, a total of 2×10^8 primary histories were simulated to ensure sufficient statistical precision. The beam geometry was defined as a field size of 10×10 cm^2 at an SSD of 100 cm. Regarding transport parameters, the global cutoff energies were set to 0.7 MeV for electrons (ECUT) and 0.01 MeV for photons (PCUT) [31,32]. To optimize computational efficiency, electron range rejection was employed with ESAVE values of 2 MeV, 4 MeV, and 6 MeV for the 6, 9, and 16 MeV beams, respectively.

2.1.2.2. Beam model validation

To validate the MC model, we compared simulated PDD in a water phantom against standard benchmarks. We referenced IAEA phase-space data for the Varian Clinac 2100C [30] for the 6 and 9 MeV beams. The comparison result for the 9 MeV results is illustrated in Figure 1. For the 16 MeV beam, validation involved comparing simulated depth-dose parameter against clinical values from the IAEA TRS-398 protocol [33]. The results showed strong agreement; most notably, the simulated R_{50} values deviated by less than 0.7% from the calculated clinical values. This consistency across energy levels confirms the accuracy of beam modeling.

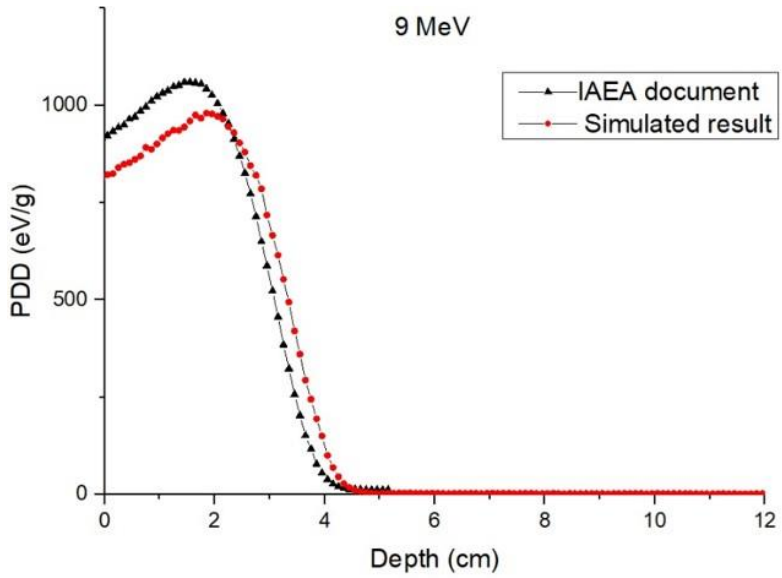

Figure 1. Comparison of simulated and reference PDD curves, benchmark data obtained from the Varian IAEA phase-space database.

2.1.2.3. Beam quality

Beam quality specifications were assessed following the IAEA TRS 398 protocol [33]. Key parameters included the water depth at half-maximum dose R_{50}, most probable energy, and full width at half maximum (FWHM). The specifications of the applied electron beams were summarized in Table 2. Dosxyznrc [34] calculated the dose (where we get R_{50}), whereas BEAMDP analyzed the beam data/phase space (where we get FWHM and Energy) [35].

2.1.3. Dose measurement

2.1.3.1. DOSXYZnrc code

The DOSXYZnrc code was used to simulate the interaction between the electron beams and the experimental setup (phantom, bolus and shield) as shown in Figure 2. The PEGS4 file was used to model material properties, while the phase-space files generated from BEAMnrc served as the source of electron particles. A summary of MC input parameters is presented in Table 3.

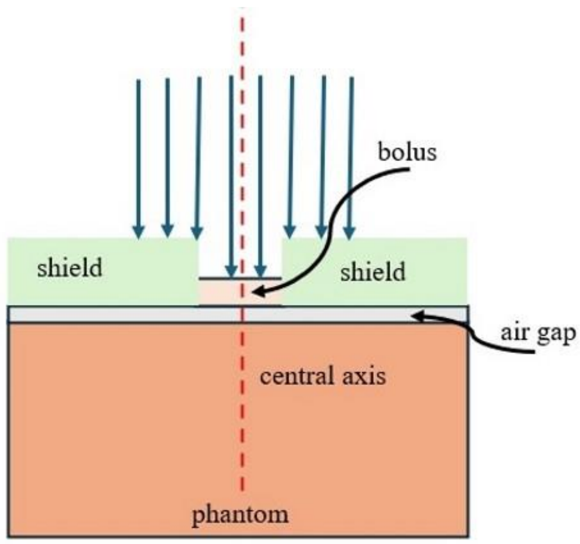

Figure 2. Schematic diagram of the phantom and shielding assembly setup exposed to the electron beam.

2.1.3.2. Rotational sensitivity

In the model configuration shown in Figure 2, we assumed the electron source was mono-directional and normally incidence (0° deviation), directed upon the setup. Since perfect normal incidence is an idealization rarely achieved in actual clinical practice, we assessed the model's sensitivity to potential setup errors. We ran supplementary simulations with the beam incidence angled at $\pm 5°$ and $\pm 10°$ relative to the surface normal. This allowed us to quantify the dosimetric impact of angular misalignments. The acquired PDDs were compared in terms of SD, R_{90}, and R_{50} values with the baseline calculation assumptions of 0° deviation. For this assessment, we selected a representative case: the 9 MeV beam delivered through a 5×5 cm^2 aperture with a 0.5 cm ABS bolus and the proposed shielding materials described in the next section.

Table 2. Characteristics of the applied electron beam radiation.

Nominal energy (MeV)	6*	9*	16**
Energy peak (MeV)	6.67	9.23	14.6
FWHM (cm)	0.17	0.3	0.57
R_{50} (cm)	2.56	3.7	5.6

* Varian 2100C, ** Philips Sl75-20

2.2. Model configuration

Boluses of ABS with varying dimensions of ($2 \times 2\ cm^2, 5 \times 5\ cm^2,$ and $8 \times 8\ cm^2$) with a uniform thickness of 0.5 cm were positioned over the PTV on the phantom surface. A shield with an aperture matching the bolus area dimensions was placed over the phantom surface to encompass the bolus. The shield was constructed from one of the following materials: PLA, ABS, or lead alloy. The thickness of each shield material was determined based on the incident beam radiation and the material's density. Although the ESTAR database provides reference values, it reports on the CSDA range (the length of the microscopic track the electron follows before coming to rest). Relying solely on this can lead to an overestimation of the required thickness, as the actual depth of penetration is shorter than the total track length. Since our study investigates low-density materials like ABS and PLA, we adopted the values from Equation (1) as the minimum thickness for effective shielding [1], where it provides the geometric shielding thickness (R_{max}) specifically required to stop the electrons. For experimental work (as opposed to simulation), we recommend adding a safety margin of approximately 2 mm to ensure complete blockage and prevent dose leakage.

Table 3. Summary of MC parameter settings used in DOSXYZnrc code.

Physics parameter	Setting/Source
Electron cutoff energy	0.521 MeV
Photon cutoff energy	0.01 MeV
Number of histories	2×10^8
Transport_algorithm	PRESTA-II
ESAVE (MeV)	2, 4 and 6*
Photon Cross- Sections	NIST XCOM
Bremsstrahlung/Pair Production Cross-Sections	Bethe-Heitler (BH)
Bound Compton Scattering	Enabled
Rayleigh Scattering	Enabled
Atomic Relaxations	Enabled

* 2 for 6 MeV, 4 for 9 MeV, and 6 for 16 MeV.

The ABS and PLA shield materials were chosen due to their widespread use in bolus fabrication by 3D printing technology. This facilitated the creation of custom-shaped shields and bolus structures with varying thicknesses, offering flexibility in design and reducing the need for multiple, separate shield pieces. Lead was compared with ABS and PLA and served as the performance benchmark [1,36–38].

$$R_{max}(mm) = \frac{5.42 \times (energy\ of\ electron\ beam\ MeV) - 1.33}{density\ of\ shielding\ material} \quad (1)$$

The measurements were performed on a $30 \times 30 \times 30\ cm^3$ solid water phantom covered with a custom bolus-shield cover (Figure 2). The bolus and shield thicknesses denoted (a) and (b), respectively, were chosen for each electron energy as outlined in Table 4. Bolus thickness was fixed at 0.5 cm in all cases. Shield thicknesses were selected based on the corresponding R_{max} values. The values obtained from Equation (1) were rounded to the nearest 0.1 cm and are presented in Table 4. These rounded values were used to model the shield thickness in the simulation geometry. A 0.3 cm air gap was introduced between the shielding assembly (bolus and shield) and phantom for more realistic clinical situations. A focused analysis was conducted to investigate the effect of air gap size (0, 3, 5 mm). The results indicate that a 3 mm and 5 mm gap causes the surface dose to increase only slightly (3%) compared to the ideal zero-gap geometry. However, at deeper depths, the discrepancy caused by the 3 mm gap is more pronounced, showing a shift of approximately 0.1−0.3 cm. This deviation was even larger for the 5 mm gap, where shifts in R_{90} and R_{50} ranged from 0.4 to 0.7 cm. These findings confirm that while the air gap largely preserves the surface dose, it notably alters the position of the dose at the target depth. Our selection of a 3 mm air gap is justified, as it simulates a realistic clinical scenario. We deliberately avoided using an ideal (0 mm) or excessively large gap to ensure the experimental setup reflects practical treatment conditions.

Table 4. Bolus- shield materials and thicknesses used.

	6 MeV		9 MeV		16 MeV	
	a	*b*	*a*	*b*	*a*	*b*
Lead		0.3		0.5		0.9
PLA	0.5	2.5	0.5	3.8	0.5	6.8
ABS		3.5		5.3		9.5

a: Bolus (ABS), b: shield thickness (cm).

Table 4 presents the simulation scenarios conducted in this study. Each scenario was repeated for three distinct bolus areas : $2 \times 2\ \mathrm{cm}^2, 5 \times 5\ \mathrm{cm}^2$, and $8 \times 8\ \mathrm{cm}^2$. In addition, a reference simulation was conducted for each beam energy, employing a 0.5 cm thick ABS bolus that covered the entire phantom surface. This reference measurement serves as a benchmark to assess the impact of shielding material choice on the depth dose at the central axis (CAX).

MC simulations were performed using DOSXYZnrc to calculate depth doses at the CAX and lateral profiles. Data analysis and visualization were carried out using StatDose and Origin software.

3. Results

The dosimetric effects of the proposed shielding configuration were evaluated across varying electron beam energies. Figure 3 highlights the results for the 9 MeV setup, comparing the lead shield configuration (3a) with the PLA shield (3b). The interaction between the bolus, shield, and phantom is clearly illustrated by the color-coded isodose curves, which range from 100% to 5%. These curves reveal the radiation penetration pattern, offering a clear perspective on how effectively the shielding assembly modulates the dose at varying depths.

The figure also illustrates the relative dimensions of the shield and bolus. While the ABS bolus remains a consistent 0.5 cm in both cases, there is a distinct difference in the shields: the lead shield in Figure 3a is 0.3 cm thick, whereas the PLA shield in Figure 3b is 2.5 cm. This increased thickness in the PLA setup creates a deep "tunnel" for the beam, significantly influencing the resulting dose distribution. Furthermore, these images allow for the precise detection of hot spots through a detailed, pixel-by-pixel examination.

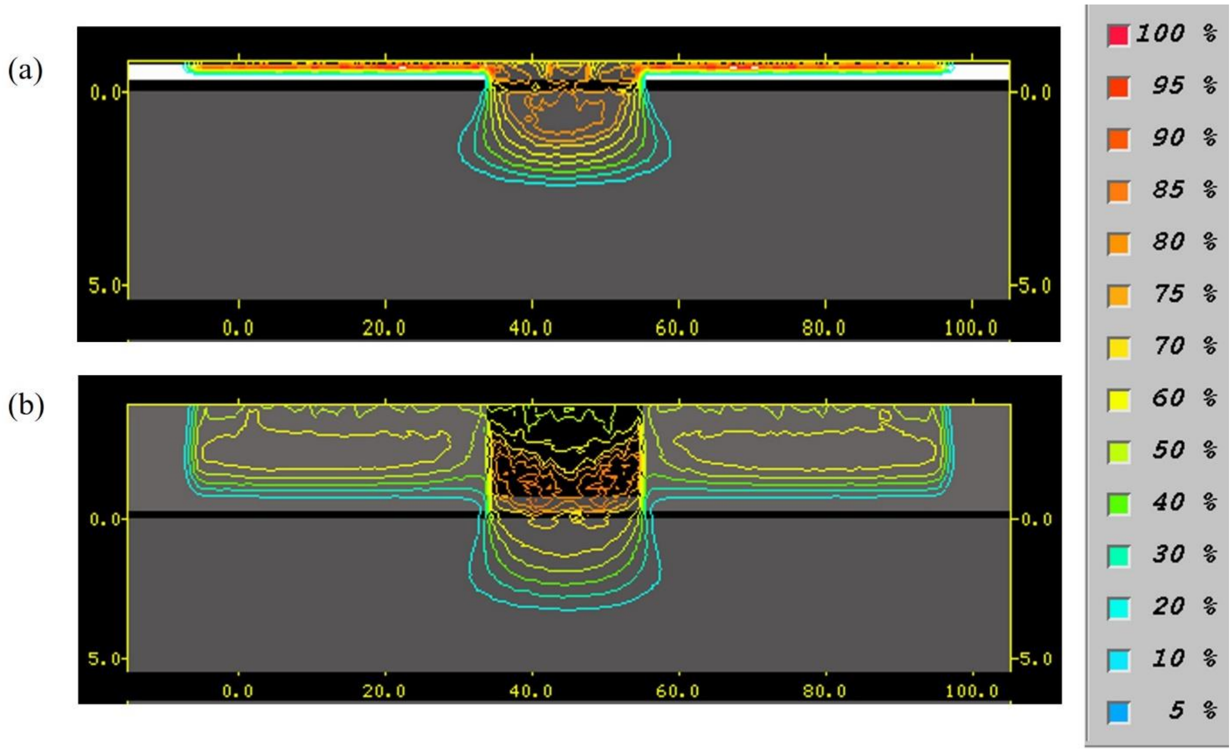

Figure 3. Isodose curves in the X-Z plane for a 9 MeV electron beam incident on the 2 × 2 cm^2 ABS bolus configuration with (a) lead shielding and (b) PLA shielding. The color scale on the right indicates the relative dose percentage.

Figures 4 to 6 illustrate depth dose distributions at the CAX for the three irradiation energies. The data were categorized by shield aperture area. The relative surface dose (RSD) values were extracted from these profiles and were summarized in Table 5. The simulation was performed using 2×10^8 initial histories to ensure high statistical precision. The resulting statistical uncertainty was tracked throughout the phantom. For the target volume/region of interest, the maximum relative standard deviation for surface dose was about 2%, and for the dose depths, near and beyond d_{max}, the uncertainty was approximately 1%. These values confirm that the 2×10^8 histories were sufficient to achieve an acceptable statistical uncertainty for the MC simulation.

3.1. The impact on surface dose

Figure 4 shows the impact of a small, 2 × 2 cm^2 shield aperture irradiated with 6, 9, and 16 MeV electron beams. For 6 and 9 MeV (Figure 4a and 4b), ABS and PLA shields consistently resulted in a higher dose compared to the lead shield up to a depth of approximately 0.6 and 0.9 cm, respectively. For 16 MeV (Figure 4c), lead showed increased dose at the surface. Table 5 presents the RSD, which quantifies the percentage change in surface dose (SD) for each simulation relative to the benchmark reference SD, calculated using the following formula:

$$RSD\% = \frac{\left(SD - SD_{ref}\right)}{SD_{ref}} \times 100\% \quad (2)$$

Figure 5 illustrates the effect of a 5 × 5 cm^2 shield aperture on depth dose profile. As shown in Figure 5a, the 6 MeV irradiation had a minimal effect on the central axis depth dose. However, for 9 and 16 MeV energies (Figure 5b and 5c), the ABS and PLA shields resulted in an enhanced surface dose up to a depth of 0.9 cm compared to the lead shield. Additionally, Table 5 shows that ABS and PLA shields consistently exhibited a higher RSD than lead across all energy levels. In general, for these materials, the RSD increased as beam energy rose. The ABS shields proved to be an exception: when exposed to 16 MeV radiation, it demonstrates a decrease in RSD compared to its performance at 9 MeV. Figure 6 displays the CAX dose profile for an 8 × 8 cm^2 shield aperture. For 6 and 9 MeV beams, the lead shield did not significantly affect the dose at CAX. However, Table 5 demonstrates that using ABS and PLA shields reduced the SD at 9 and 16 MeV, whereas the lead shield caused a slight increase in SD under 16 MeV irradiation.

3.2. Deep tissue protection

In general, across all aperture sizes, ABS and PLA shields demonstrated superior protection of deep tissues to lead. Figure 4 clearly demonstrates the effect of small shield apertures enhancing deep tissue protection, regardless of the shield material employed. Conversely, as the shield aperture size increases, this protective effect becomes less pronounced.

3.3. Dosimetric curve deviations

In Figures 4a and 4b, the ABS and PLA shields altered the reference curve from a shoulder peak to a decreasing profile, whereas the lead shield produced a plateau-like distribution. In Figure 4c, all shield materials shifted the reference curve to a decreasing profile. In Figure 5, the lead shield closely mirrored the reference curve for all beam energies. In contrast, the ABS and PLA shields maintained the original reference shape at 6 MeV, but exhibited significant changes at higher energies, evolving into a plateau-like profile at 9 MeV and a decreasing profile at 16 MeV. In Figure 6, the lead shield again closely matched the reference curve. Although the ABS and PLA shields influenced the dose along the CAX, they did not significantly alter the overall shape of the reference curve.

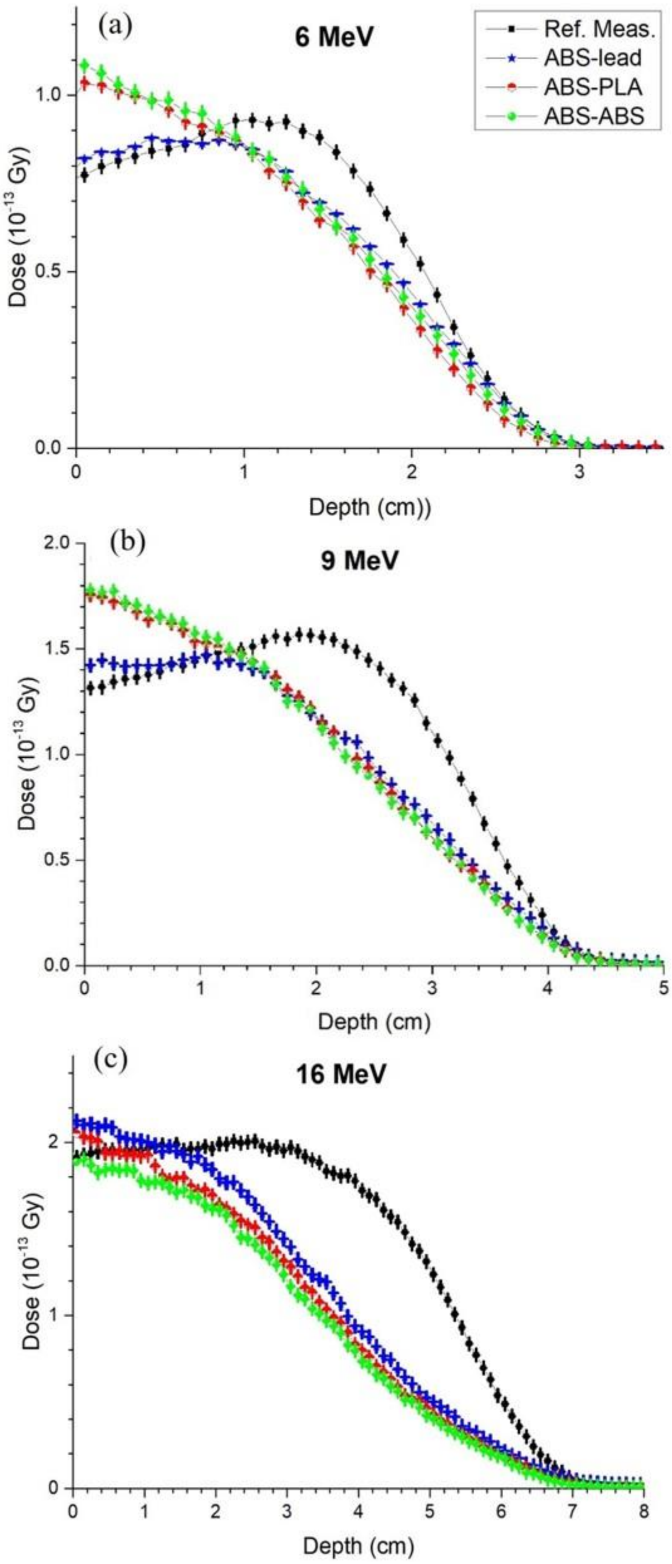

Figure 4. The depth dose profile for solid water phantom covered by different bolus-shield materials, shield aperture is 2 × 2 cm^2, irradiated by (a) 6 MeV, (b) 9 MeV, and (c) 16 MeV.

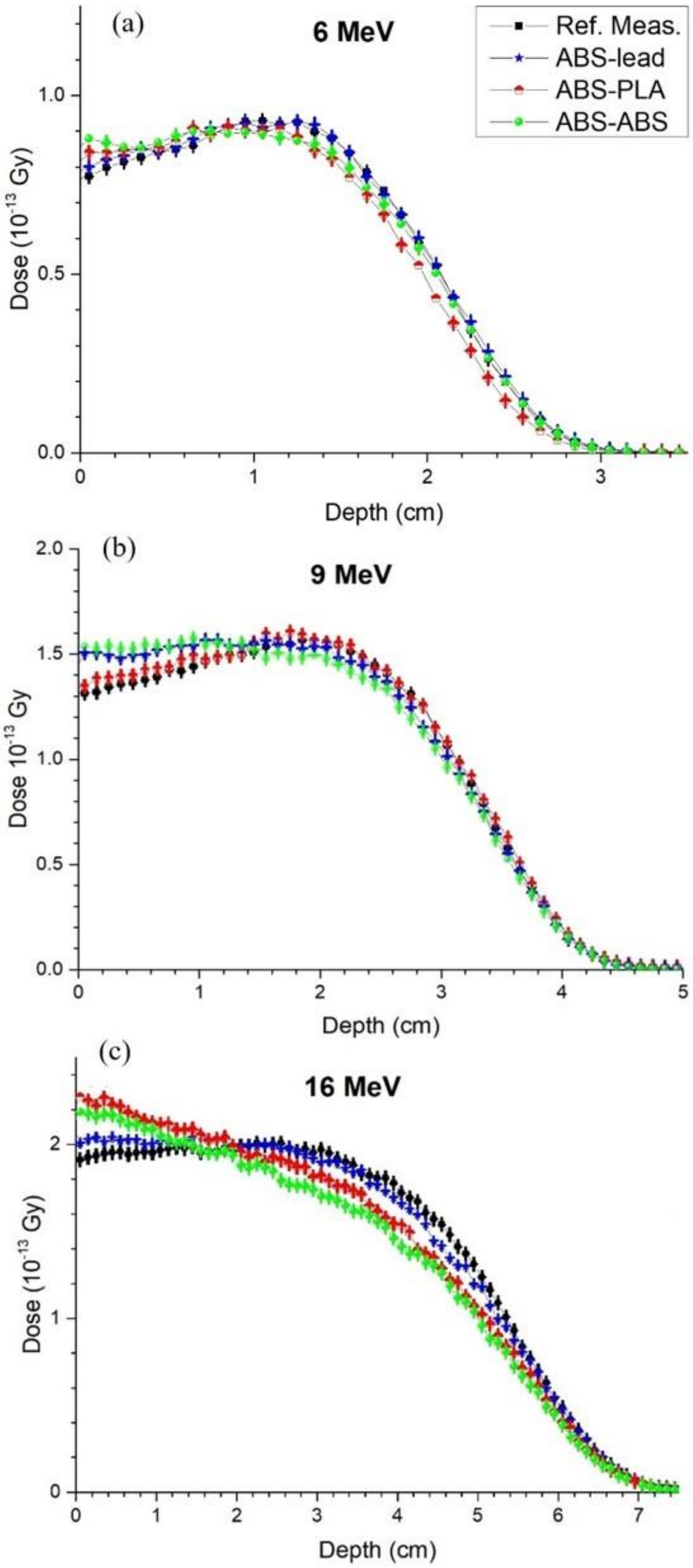

Figure 5. The depth dose profile for solid water phantom covered by different bolus-shield materials, shield aperture is 5 × 5 cm^2, irradiated by (a) 6 MeV, (b) 9 MeV, and (c) 16 MeV.

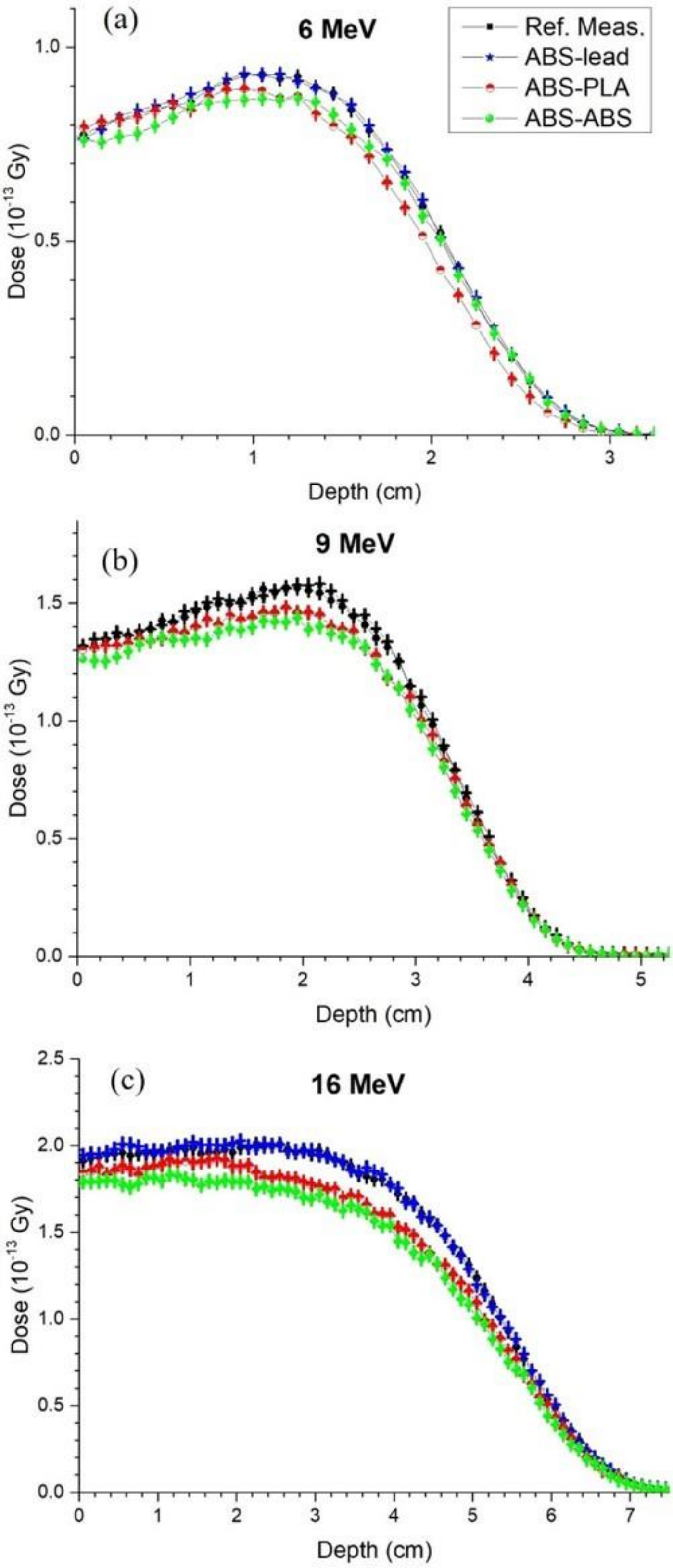

Figure 6. The depth dose profile for solid water phantom covered by different bolus-shield materials, shield aperture is 8 × 8 cm^2, irradiated by (a) 6 MeV, (b) 9 MeV, and (c) 16 MeV.

Table 5. Relative surface dose values resulting from irradiation the configuration by 6, 9, and 16 MeV electron beam energies.

RSD%									
Aperture	2×2 cm^2			5×5 cm^2			8×8 cm^2		
	6 MeV	9 MeV	16 MeV	6 MeV	9 MeV	16MeV	6 MeV	9 MeV	16 MeV
ABS	40.2	34.2	0	12.5	16.6	15.2	0	−3.7	−6.9
PLA	29.9	34.2	8.2	8.1	10.9	19.1	0	0	−3.9
Lead	5.3	8.2	12.2	2.1	3.5	7.2	0	0	2.8

3.4. The lateral dose

Figure 7 through 9 compare the lateral dose distributions for all scenarios at a depth equal d_{max}. The penumbra widths, defined as the distance between the 80% and 20% dose points, are summarized in Table 6. ABS and PLA shield materials consistently produced wider penumbras than lead. However, for each shield aperture, penumbra width decreased with increasing electron energy. Additionally, decreasing the aperture area generally resulted in a slight increase or no change in penumbra width for a given electron beam. Conversely, the effective field size, defined as the width measured at the 50% dose level, remained largely unaffected by the type of shield material used but was slightly influenced by the energy of the radiation energy, as shown in Table 6.

3.5. Rotational sensitivity

The simulations investigating the sensitivity to incident angle misalignment showed that the surface dose was insensitive to angle (Table 7), with deviations limited to a negligible range (0−0.04). The depth parameters (d_{90} and d_{50}) exhibited varying sensitivity. At a 5° tilt, shifts were minimal (0.01−0.08 cm), suggesting the model remains robust against minor misalignment. In contrast, increasing the tilt to 10° caused more pronounced deviation (0.04−0.32 cm).

4. Discussion

In radiotherapy, the selection of bolus material and thickness significantly impacts the dose delivered to the PTV. The reference measurements in Figure 4 through 6 illustrate the influence of a 0.5 cm thick ABS bolus, covering the phantom surface, on the PTV dose distribution for 6, 9, and 16 MeV electron beams in the absence of a shield. The remaining curves depict the impact of the various shield material and aperture sizes. Placing shielding materials directly on the patient's skin, as investigated in this study, influences the dose distribution along the CAX. While a shield of appropriate thickness can significantly attenuate the transmission of the primary electron beam, it can also contribute to the CAX dose through side scatter radiation [38].

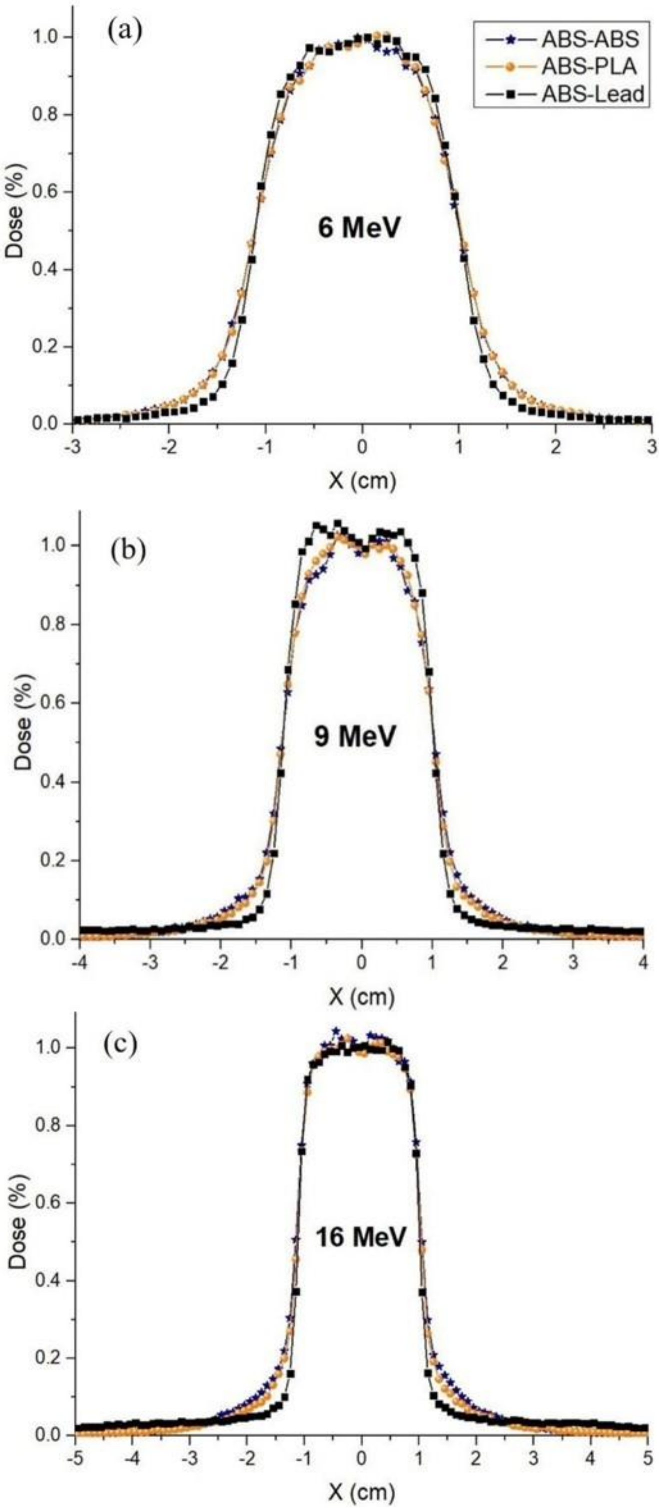

Figure 7. The lateral dose profile measured at d_{max} depth in solid water phantom covered by different bolus-shield materials, shield aperture is 2×2 cm^2, irradiated by (a) 6 MeV, (b) 9 MeV, and (c) 16 MeV.

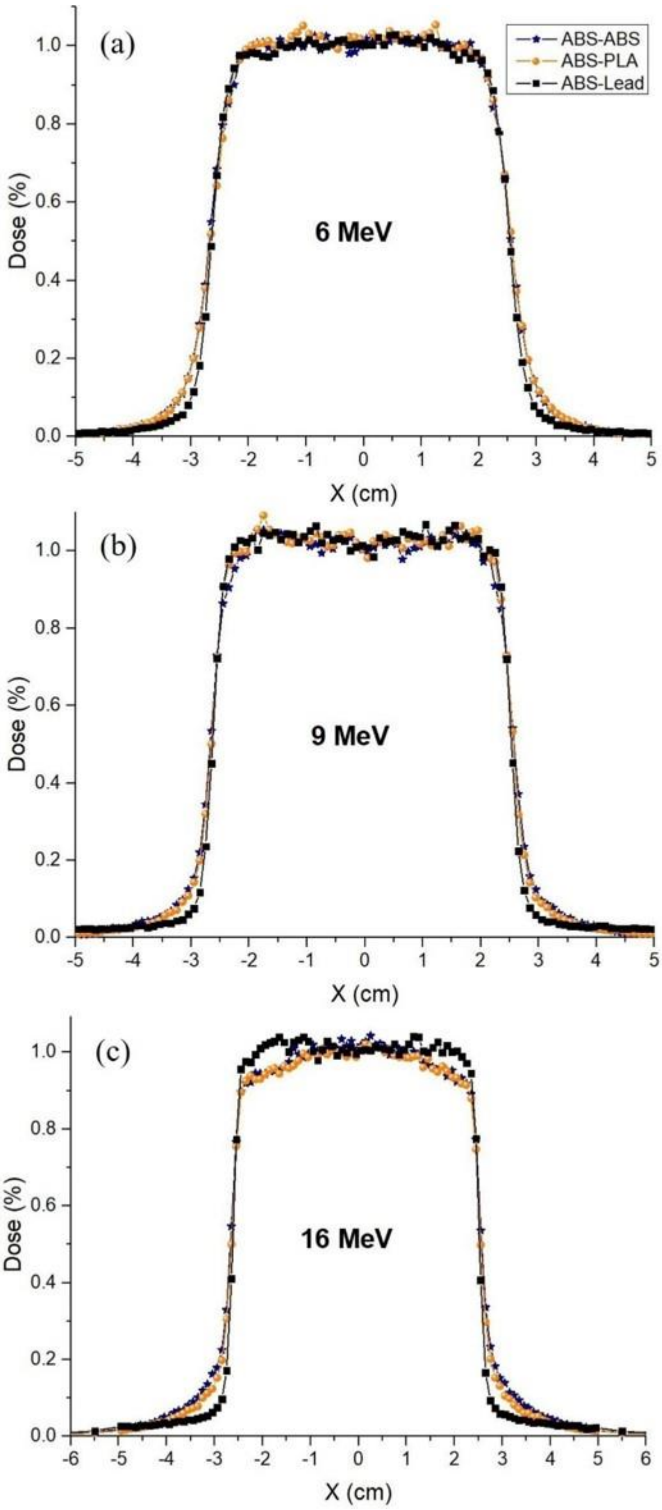

Figure 8. The lateral dose profile measured at d_{max} depth in solid water phantom covered by different bolus-shield materials, shield aperture is 5 × 5 cm^2, irradiated by (a) 6 MeV, (b) 9 MeV, and (c) 16 MeV.

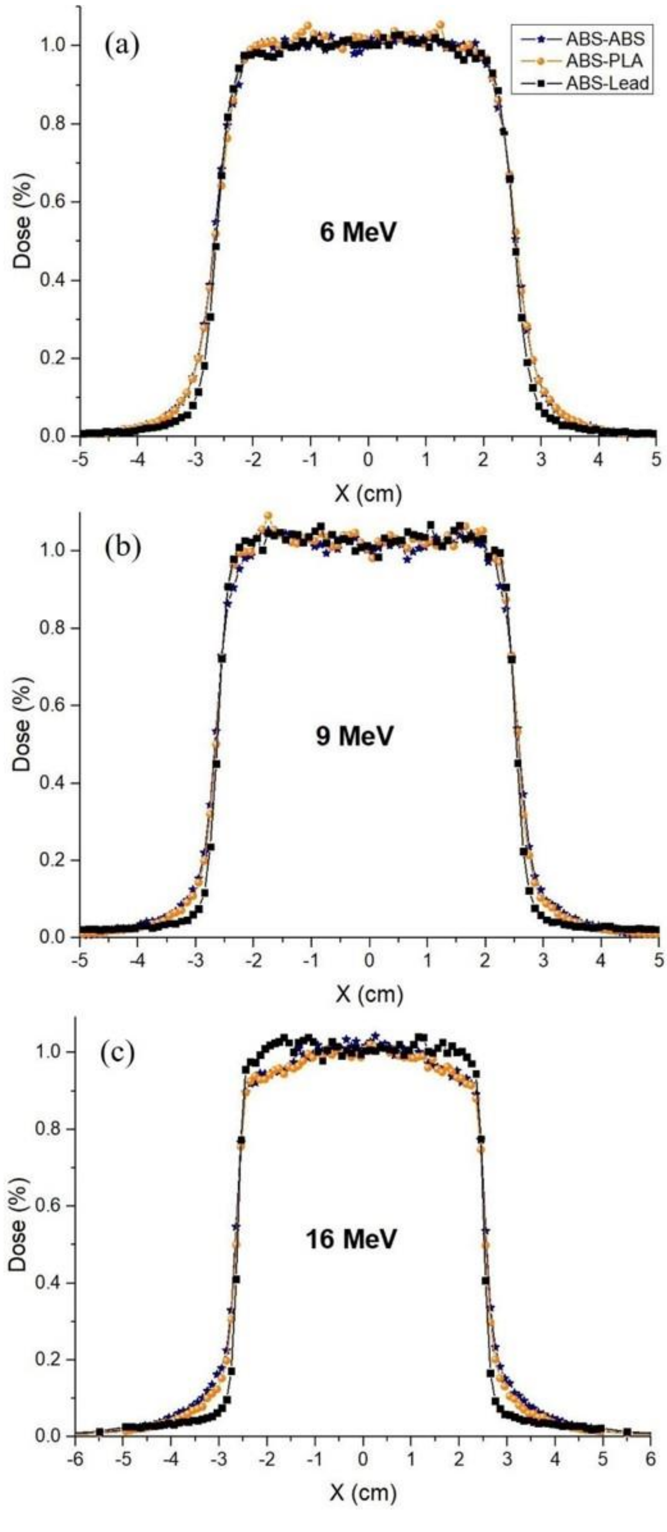

Figure 9. The lateral dose profile measured at d_{max} depth in solid water phantom covered by different bolus-shield materials, shield aperture is 8× 8 cm^2, irradiated by (a) 6 MeV, (b) 9 MeV, and (c) 16 MeV.

Table 6. Penumbra widths and effective field sizes for the lateral dose at d_{max}.

Penumbra (cm)									
Aperture	2×2 cm^2			5×5 cm^2			8×8 cm^2		
	6 MeV	9 MeV	16MeV	6 MeV	9 MeV	16MeV	6 MeV	9 MeV	16 MeV
ABS,PLA	0.57	0.46	0.33	0.60	0.36	0.34	0.52	0.36	0.35
Lead	0.39	0.26	0.19	0.50	0.25	0.2	0.36	0.23	0.15
Effective Field size (cm)									
ABS,PLA & Lead	2.13	2.13	2.18	5.2	5.19	5.2	8.3	8.21	8.19

Table 7. Sensitivity analysis of SD and depth parameters (d_{90}, d_{50}) to incident angle misalignment (± 5°, ± 10°) for different shielding configurations.

	ABS-ABS	ABS-PLA	ABS-Lead
Tilt angle	SD% ± 0.02		
0°	0.98	0.93	0.86
−5°	0.99	0.93	0.86
+5°	0.95	0.92	0.87
−10°	0.95	0.95	0.86
+10°	0.94	0.91	0.83
	d_{90} \ d_{50} (in cm) ± 0.01		
0°	2.31\3.31	2.42\ 3.32	2.44\3.36
−5°	2.29\3.26	2.38\3.29	2.50\3.38
+5°	2.30\3.29	2.40\3.29	2.52\3.40
−10°	1.99\3.11	2.46\3.20	2.60\3.40
+10°	2.00\3.15	2.24\3.24	2.60\3.41

4.1. The impact on surface dose

The sensitivity of surface dose to shielding material becomes particularly evident in the 2×2 cm^2 configuration. As detailed in Table 5, the ABS shield produced an RSD of 40.2% at 6 MeV, nearly eight times the 5.3% yielded by lead. This disparity underscores a key finding: in small-field dosimetry, the scattering power of low-density materials often matters more than the scattering power of high-Z materials.

Even though the ABS and PLA shields were manufactured to be significantly thicker (e.g., 5.3 cm and 3.8 cm for the 9 MeV beam) than the 0.5 cm lead sheet, creating an effectively deep collimating tunnel, their low-Z composition prevented them from generating effective lateral scatter as shown in the comparison between Figures 3a and 3b. This resulted in doses that were higher in the first few millimeters than at deeper depths. Without this compensatory mechanism, lateral electronic equilibrium (LEE) was lost, effectively pulling the depth of d_{max} to the surface and inflating the entrance dose. Lead, conversely, rebuilt the deep dose peak and preserved the skin-sparing build-up region.

This scattering effect explains the observed dose enhancement from the surface down to a specific depth; beyond this point, side scattering diminishes, leading to a decrease in dose. It is also notable that ABS often exhibits higher surface doses compared to PLA since PLA is denser. Thus, it requires less physical thickness to achieve the same attenuation, thereby reducing the volume of material available to scatter electrons.

For all shield materials, the RSD increases as the shield aperture decreases. This phenomenon arises because the shield edges are closer to the CAX, allowing a greater portion of side-scattered electrons to reach the CAX. For the 16 MeV electron beam (Figure 4c and 5c), a substantial 9.5 cm thick ABS shield created the deep tunnel, which was responsible for attenuating most of the scattered electrons of the beam, before they could contribute to the surface dose [4,39,40]. Consequently, the smaller aperture resulted in greater radiation attenuation due to increased collisions and interactions compared to a larger aperture. The configuration in Figure 4c resulted in greater net attenuation compared to larger aperture in Figure 5c due to the increased number of interactions within the shield. Finally, irradiating a 10 × 10 cm^2 beam through a larger 8 × 8 cm^2 aperture minimized the shielding effect, yielding results closer to the reference measurement, particularly for 6 MeV and 9 MeV beams, regardless of the material. However, for the thickest shields, specifically ABS and PLA at 16 MeV (Figure 6c) and ABS at 9 MeV (Figure 6b), the SD was slightly diminished due to the extended path length and increased thickness.

4.2. Deep tissue protection

In deep tissues, the influence of side scattering, which significantly impacts surface and near-surface regions, diminishes. Instead, the primary contributor to the dose at depth becomes bremsstrahlung radiation. Since high-atomic-number materials like lead generate more bremsstrahlung radiation than low-atomic-number materials, such as ABS and PLA, deep tissues receive a higher dose when shielded by lead. Consequently, the ABS and PLA shield offer superior protection for organs at risk located deeper in the body [38].

Furthermore, a substantial dose reduction was observed with the 2 × 2 cm^2 aperture. This is primary because the small opening significantly limits the amount of radiation penetrating the PTV. Unlike the reference setup, where a 10 × 10 cm^2 field irradiates a larger volume of the phantom and creates extensive scatter, the narrow aperture restricts the radiation surrounding the CAX, resulting in much lower total dose contribution.

4.3. Dosimetric curve deviations

The results demonstrate that combining a shield with an ABS bolus significantly reshapes the reference dose distribution, particularly for 2 × 2 cm^2 and 5 × 5 cm^2 shield apertures. A standalone 0.5 cm ABS bolus is insufficient for achieving a uniform 90% dose distribution at 6 and 9 MeV; instead, it creates dual dose hotspots that could potentially compromise healthy tissue. However, when a shield is introduced, the dose profile is modulated by the specific combination of shield type, beam energy, and aperture size. These findings allow clinicians to determine the optimal shielding conditions for specific treatment scenarios.

In general, the choice of shield material exerts a stronger influence on depth dose as shield aperture decreases. Conversely, the larger 8 × 8 cm^2 aperture had a minimal effect on the shape of the reference measurements. This suggests that for large fields, the behavior of bolus aligns with literature regarding unshielded setups and remains reliable. For instance, a 16 MeV beam can effectively treat extended tumors with a homogeneous dose over a target depth using a relatively large aperture.

However, as the aperture size increases, the lead shield exhibited a closer approximation to the reference shape, whereas the ABS and PLA shields maintain a slight deviation from the ideal reference profile. These persistent differences are attributed to the specific factors influencing surface dose and deep tissue protection, as discussed previously.

4.4. The lateral dose

The lateral dose profiles presented in Figure 7 through 9 were measured at d_{max}. At this depth, the dose at the CAX is notably higher for ABS and PLA shields compared to lead. This elevation is driven by the increased side scattering characteristic of these lower-atomic-number materials, as illustrated above. Consequently, the lateral dose profile for ABS and PLA are broader, resulting in a wider penumbra at this depth compared to the lead shield.

Furthermore, with low-energy beams, electrons significantly deviate from their original trajectories upon interacting with matter, which broadens the beam profiles. However, as beam energy increases, particles are less likely to undergo large-angle deflection, resulting in more forward-focused beam. This reduction in lateral scattering explains the observed decrease in penumbra width as the energy increase.

We also observed a slight increase in penumbra width as the shield aperture size decreased. This is likely due to the proximity of the shield edges to the CAX; as the aperture narrows, the scattering material is physically closer to the measurement field, contributing more scattered radiation and broadening the lateral dose distribution.

Our findings regarding effective field size align with established literature. As expected, the choice of shield material had minimal impact on the effective field size [1], which is primarily determined by the geometric setup. However, as indicated in Table 6, increasing the beam energy did lead to a larger effective field size. This expansion is primarily attributed to the increased lateral range of the electrons and potential transmission through the edges of the aperture shield.

4.5. Rotational sensitivity

The sensitivity analysis confirms that our model is robust enough to handle the minor angular misalignment often encountered in the clinic. Since deviation at a 5° tilt was negligible, we can be confident that standard setup errors, usually contained within $\pm$ 3°, will not compromise dosimetric accuracy [5]. Consequently, while the system performs reliably for standard perpendicular setup, we advise caution if the beam angle is expected to deviate by more than 5°.

5. Conclusions

This study demonstrates the substantial impact of shield material on the CAX dose distribution when used in conjunction with a bolus. Our findings highlight the critical role of material selection, radiation energy, and shield aperture size in determining the resulting dose profile.

Specifically, we demonstrated that ABS and PLA, commonly used in 3D-bolus fabrication, can effectively serve as shield materials for low and medium electron beam energies. Although they require greater physical thickness than high-density materials like lead, they offer distinct advantages for small aperture shields (e.g., 2×2 cm^2 and 5×5 cm^2).

Key benefits include surface dose enhancement, superior protection of deeper tissues, and the ability to reshape the dose profile to eliminate the misalignment issues often encountered with traditional separate components, ensuring better adherence to the skin and improved treatment accuracy. However, the use of ABS or PLA for high energy beams, such as 16 MeV, is less practical due to the substantial thickness required and their impact on the surface dose region, where these materials may either reduce the surface dose or cause only minor enhancements. This study also reveals that the dosimetric behavior of a bolus changes significantly depending on the shield aperture area. This suggests that the standard dosimetric characteristics established in the literature are most reliable for large shield apertures (greater than 5×5 cm^2), whereas small-field scenarios require the specific consideration highlighted in this work.

Finally, our analysis confirms the model is robust against standard setup errors error, with negligible deviation up to $\pm 5°$. Beyond this, the obliquity effect compromises accuracy. Thus, we advise limiting angular misalignment to a maximum of 5° for reliable results.

Use of generative-AI tools declaration

The author declares she has not used Artificial Intelligence (AI) tools in the creation of this article.

Conflict of interest

The author declares no conflict of interest.

Author contributions

The author is solely responsible for all aspects of this research, including the study's conception, design, methodology, data acquisition, analysis, interpretation, and the writing of the manuscript.

References

1. Kijima K, Monzen H, Matsumoto K, et al. (2018) The shielding ability of novel tungsten rubber against the electron beam for clinical use in radiation therapy. *Anticancer Res* 38: 3919–3927. https://doi.org/10.21873/anticanres.12677
2. Wakabayashi K, Monzen H, Tamura M, et al. (2021) Dosimetric evaluation of skin collimation with tungsten rubber for electron radiotherapy: a Monte Carlo study. *J Appl Clin Med Phys* 22: 63−70. https://doi.org/10.1002/acm2.13210
3. Lucido III JJ, Veres AJ, Kehret SM, et al. (2022) Development of transparent eye shields for total skin electron beam radiotherapy. *J Appl Clin Med Phys* 23: e13722. https://doi.org/10.1002/acm2.13722
4. Alhamada H, Simon S, Philippson C, et al. (2020) Monte Carlo dose calculations of shielding disks with different material combinations in intraoperative electron radiation therapy. *IOERT Cancer/Radiothérapie* 24: 128−134. https://doi.org/10.1016/j.canrad.2020.02.006

5. Khan FM, Gibbons JP (2019) *The Physics of Radiation Therapy*, 5 Eds., Philadelphia: Lippincott Williams & Wilkins, 256–305.
6. Vyas V, Palmer L, Mudge R, et al. (2013) On bolus for megavoltage photon and electron radiation therapy. *Med Dosi* 38: 268–273. https://doi.org/10.1016/j.meddos.2013.02.007
7. Diaz-Merchan JA, Español-Castro C, Martinez-Ovalle SA, et al. (2023) Bolus 3D printing for radiotherapy with conventional PLA, ABS and TPU Filaments: theoretical-experimental study. *Appl Radiat Isot* 199: 110908. https://doi.org/10.1016/j.apradiso.2023. 110908
8. Diaz-Merchan JA, Martinez-Ovalle SA, Vega-Carrillo HR (2023) Development of a 3D printing process of bolus using bolus CM material for radiotherapy with electrons. *Appl Radiat Iso* 199: 110899. https://doi.org/10.1016/j.apradiso.2023.110899
9. Moghaddam SHZ, Baghani HR, Mahdavi SR (2020) Construction and performance valuation of a buildup bolus for breast intraoperative electron radiotherapy. *Radiat Phys Chem* 174: 108952. https://doi.org/10.1016/j.radphyschem.2020.108952
10. Wang X, Wang X, Xiang Z, et al. (2021) The clinical application of 3D-printed boluses in superficial tumor. *Front Oncol* 11: 698773. https://doi.org/10.3389/fonc.2021.698773
11. Zou W, Fisher T, Zhang M, et al. (2015) Potential of 3D printing technologies for fabrication of electron bolus and proton compensators. *J Appl Clin Med Phys* 16: 90–98. https://doi.org/10.1120/jacmp.v16i3.4959
12. Łukowiak M, Jezierska K, Boehlke M, et al. (2017) Utilization of a 3D printer to fabricate boluses used for electron therapy of skin lesions of the eye canthi. *J Appl Clin Med Phy* 18: 76–81. https://doi.org/ /10.1002/acm2.12013
13. Lee VW, Liu AC, Cheng KW, et al. (2023) Dosimetric benefits of 3D-printed modulated electron bolus following lumpectomy and whole-breast radiotherapy for left breast cancer. *Med Dosim* 48: 37−43. https://doi.org/10.1016/j.meddos.2022.10.001
14. Herchko SM, Rutenberg MS, Beltran CJ, et al. (2024) A comparison of in-house 3D-printed and commercially available patient-specific skin collimators for use with electron beam therapy. *J Appl Clin Med Phys* 25: e14366. https://doi.org/10.1002/acm2.14366
15. Kawai Y, Tamura M, Amano M, et al. (2019) Dosimetric characterization of a novel surface collimator with tungsten functional paper for electron ttherapy. *Anticancer Res* 39: 2839–2843. https://doi.org/10.21873/anticanres.13412
16. Chow JCL, Grigorov GN (2009) Dosimetric dependence of the dimensional characteristics on a lead shield in electron radiotherapy: a Monte Carlo study. *J Appl Clin Med Phys* 10: 75–91. https://doi.org/10.1120/jacmp.v10i2.2918
17. Russo S, Bettarini S, Grilli Leonulli B, et al. (2022) Dosimetric characterization of small radiotherapy electron beams collimated by circular applicators with the new microsilicon detector. *Appl Sci* 12: 600. https://doi.org/10.3390/app12020600
18. Han SC, Han MC, Kim J, et al. (2025) Feasibility study for dose calculation with a radiation treatment planning system using a fixed-size electron cone applicator for small electron fields. *Plos One* 20: e0324722. https://doi.org/10.1371/journal.pone.0324722
19. Gerbi BJ, Antolak JA, Deibel FC, et al. (2009) Recommendations for clinical electron beam dosimetry: Supplement to the recommendations of Task Group 25. *Med Phys* 36: 3239−3279. https://doi.org/10.1118/1.3125820
20. Kong D, Wu J, Kong X, et al. (2024) Effect of bolus materials on dose deposition in deep tissues during electron beam radiotherapy. *J Radiat Res* 65: 215−222. https://doi.org/10.1093/jrr/rrae001

21. Diaz-Merchan JA, Martinez-Ovalle SA, Vega-Carrillo HR (2022) Characterization of a novel material to be used as bolus in radiotherapy with electrons. *Appl Radiat Iso* 183: 110154. https://doi.org/10.1016/j.apradiso.2022.110154
22. Tamura M, Monzen H, Kubo K, et al. (2017) Feasibility of tungsten functional paper in electron grid therapy: a Monte Carlo study. *Phys Med Biol* 62: 878–889. https://doi.org/10.1088/1361-6560/62/3/878
23. Okuhata K, Tamura M, Monzen H, et al. (2021) Dosimetric characteristics of a thin bolus made of variable shape tungsten rubber for photon radiotherapy. *Phys Eng Sci Med* 44: 1249−1255. https://doi.org/10.1007/s13246-021-01059-2
24. Makrani DS, Nedaei HA, Geraily G, et al. (2024) Monte Carlo simulation for the Radixact™ tomotherapy linac using EGSnrc. *J Med Phys* 49: 379−386. https://doi.org/10.4103/jmp.jmp_29_24
25. Kawrakow I, Rogers DWO, Mainegra-Hing E, et al. (2000) EGSnrc toolkit for Monte Carlo simulation of ionizing radiation transport. National Research Council of Canada. Available from: https://github.com/nrc-cnrc/EGSnrc.
26. National Institute of Standard and Technology Stopping Power and Range Tables for Electrons Nist. gov. Available from: https://physics.nist.gov/PhysRefData/Star/Text/ESTAR.html.
27. Rogers DWO, Faddegon BA, Ding GX, et al. (1995) BEAM: a Monte Carlo code to simulate radiotherapy treatment units. *Med Phys* 22: 503–524. http://doi.org/10.1118/1.597552
28. Rogers DWO, Walters B, Kawrakow I (2009) BEAMnrc users manual. National Research Council Canada. Institute for National Measurement Standards, PIRS-0509a (revL), Ottawa, Canda. Available from: https://nrc-cnrc.github.io/EGSnrc/doc/pirs509a-beamnrc.pdf.
29. Udale M (1988) A Monte Carlo investigation of surface doses for broad electron beams. *Phys Med Biol* 33: 939–953. https://doi.org/10.1088/0031-9155/33/8/004
30. International Atomic Energy Agency Phase space database for external beam radiotherapy. Available from: https://www-nds.iaea.org/phsp/phsp.htmlx.
31. Tuğrul T and Eroğul O (2019) Determination of initial electron parameters by means of Monte Carlo simulations for the Siemens Artiste Linac 6MV photon beam. *Rep Pract Oncol Radiother* 24: 331−337. https://doi.org/10.1016/j.rpor.2019.05.002
32. Tuğrul T (2021) Effect of different target materials of LINAC head on photon spec-trum. *J Radiat Res Appl Sci* 14: 204−209. https://doi.org/10.1080/16878507.2021.1921964
33. International Atomic Energy Agency (2000) *Absorbed Dose Determination in External Beam Radiotherapy: an International Code of Practice for Dosimetry Based on Standards of Absorbed Dose to Water*. Vienna : International Atomic Energy Agency.
34. Walters B, Kawrakow I, Rogers DWO (2005) DOSXYZnrc users manual. National Research Council Report PIRS-794 Ottawa, Canda. Available from: https://nrc-cnrc.github.io/EGSnrc/doc/pirs794-dosxyznrc.pdf.
35. Ma CM, Rogers DWO (1995) BEAMDP users manual. National Research Council Report PIRS-0509 (C) rev. A. Ottawa, Canda. Available from: https://nrc-cnrc.github.io/EGSnrc/doc/pirs509c-beamdp.pdf.
36. Verhaegen F, Buffa FM, Deehan C (2001) Quantifying effects of lead shielding in electron beams: a Monte Carlo study. *Phys Med Biol* 46: 757–769. https://doi.org/10.1088/0031-9155/46/3/311

37. Monzen H, Tamura M, Kijima K, et al. (2019) Estimation of radiation shielding ability in electron therapy and brachytherapy with real time variable shape tungsten rubber. *Phys Med* 66: 29–35. https://doi.org/10.1016/j.ejmp.2019.09.233
38. Fujimoto T, Monzen H, Nakata M, et al. (2014) Dosimetric shield evaluation with tungsten sheet in 4, 6, and 9MeV electron beams. *Phys Med* 30: 838–842. https://doi.org/10.1016/j.ejmp.2014.05. 009
39. Baghani HR, Robatjazi M, Mahdavi SR (2020) Comparing the performance of some dedicated radioprotection disks in breast intraoperative electron radiotherapy: a Monte Carlo study. *Radiat Environ Biophys* 59: 265–281. https://doi.org/10.1007/s00411-020-00836-z
40. Chow JCL (2008) Monte Carlo simulation of backscatter from lead for clinical electron beams using EGSnrc. *Med Phys* 35: 1241–1250. https://doi.org/10.1118/1.2874552